Electrochemical performance of nanosized MnO 2 synthesized by redox route using biological reducing agents

Hanaa M Abuzeid, Ahmed M Hashem, Maximilian Kaus, Michael Knapp, Sylvio Indris, Helmut Ehrenberg, Alain Mauger, Christian M. Julien

Electrochemical performance of nanosized MnO_2 synthesized by redox route using biological reducing agents

Hanaa M. Abuzeid[1], Ahmed M. Hashem[1], Maximilian Kaus[2], Michael Knapp[2], Sylvio Indris[2], Helmut Ehrenberg[2], Alain Mauger[3], Christian M. Julien[3,*]

[1]National Research Centre, Inorganic Chemistry Department, 33 El Bohouth St. (former El Tahrir St.), Dokki, Giza, Egypt, P.O.12622

[2]Karlsruhe Institute of Technology (KIT), Institute for Applied Materials (IAM), Hermann-von-Helmholtz-Platz 1, D-76344 Eggenstein-Leopoldshafen, Germany

[3]Sorbonne Université, UPMC Univ. Paris6, Institut de Minéralogie, de Physique des Matériaux et de Cosmochimie (IMPMC), UMR 7590, 4 place Jussieu, 75005 Paris, France

***Corresponding author:** E-mail : Christian.Julien@upmc.fr

Keywords: Lithium-ion batteries; α-MnO_2; Green tea; Black tea; Polyphenols; Cathode materials.

ABSTRACT

For more than a century, manganese dioxides (MDOs) have been used as electrochemically active materials in energy storage and conversion applications. To reduce the cost and hazardous impact of synthesis, a redox method was used to prepare MnO_2 using extracts of green (GT-MnO_2) and black (BT-MnO_2) tea as biological reducing agents. Polyphenols present in the extracts of tea not only reduce Mn^{7+} ions but also act as "capping agents" to stabilize and prevent the produced MnO_2 nanoparticles from degradation and aggregation. Elemental, structural properties and morphology of nanosized α-K_xMnO_2 were studied by thermogravimetric analysis, X-ray powder diffraction and Raman spectroscopy, which revealed the different crystallinity between GT-MnO_2 and BT-MnO_2 due to the strength of the antioxidant species. Electrochemical investigations highlight the beneficial presence of K^+ ions in (2×2) tunnels; with a higher concentration, α-$K_{0.135}MnO_2$ exhibits a discharge specific capacity of 155 mAh g^{-1} after 20 cycles at C/26 rate.

1. Introduction

Great interests have been directed towards developing new energy storage and conversion systems to overcome the expected lack of fossil fuels and to alleviate the environmental problems [1, 2]. The rechargeable lithium-ion battery is one of the most important and effective batteries for supplying energy [3,4]. Therefore, great efforts have been made to develop new electrode materials for the next generation of lithium-ion batteries having high energy and power density and excellent cycling performance to satisfy market demands [3,5,6].

Low cost, high theoretical capacity, environmental friendliness, and natural abundance are the main advantages of manganese dioxides, MnO_2 (MDOs), which make them promising electrode materials for lithium-ion batteries and supercapacitors [7,8]. However, the practical application of MnO_2 as electrode material for lithium-ion batteries is actually limited by the poor conductivity, large volume expansion and aggregation during Li insertion/extraction, which limits its rechargeability. Brousse et al. [9] reported electronic and ionic conductivities of 0.009 and 0.01 S cm^{-1}, respectively, for cryptomelane compared to ~6×10^{-6} and 0.015 S cm^{-1}, respectively, for birnessite. That is why composite materials of MnO_2 have been fabricated with various conducting materials (see [10] for a review). In particular, MnO_2@TiO_2 composite used as an anode recently delivered a capacity of 802 mAh g^{-1} at the current rate of 200 mA g^{-1} after 200 cycles, and still retained 400 mA h g^{-1} at a higher current rate of 1 A g^{-1} [11]. Three-dimensional $ZnFe_2O_4$@MnO_2 hierarchical core/shell nanosheet arrays as battery-type electrode exhibit high capacity of 1084 C g^{-1} at current density of 2 A g^{-1} with coulombic efficiency of 96.1% after 5000 cycles [12]. Recent MnO_2-based composites including MnO_2/carbon, MnO_2/graphene, MnO_2 nanowires@$Ni_{1-x}Co_xO_y$ heterostructures, $CoMoO_4$@C@MnO_2 core-shell structures and MnO_2/carbonized cotton textile hybrids have been developed as electrodes in supercapacitors [13-17].

Different MDO polymorphs such as α-, β-, γ- and δ-MnO_2 phases with various morphologies including nanorods, nanowires, nanosheets and nanobelts have been investigated to get better electrochemical performance [18–20]. To control the crystallite size, degree of crystallinity, the morphology, and specific surface area, the preparation method should be chosen carefully. A recent example is provided by the synthesis of nanosheet-based MnO_2

hollow capsules, which delivered a capacity of 1182.9 mAh g^{-1} for the initial cycle and 198.4 mAh g^{-1} after 500 cycles [21]. Numerous methods to synthesize MnO_2 include sol-gel [22], hydrothermal methods [23-25], refluxing method [26] and wet-chemical methods [27-31]. For most of them, strong mixing, long time and high temperature are required, resulting in the waste of a lot of energy [32,33]. It is then desirable to develop facile, cheap, environmentally benign, and size control routes to prepare MnO_2 nanoparticles [34]. In particular, biogenic approaches for the preparation of nanomaterials can be a good alternative to achieve the advantages mentioned above [35]. Non-hazardous chemicals, biodegradable polymers, available fruits, vegetables, herbs containing high concentration of polyphenols can act as antioxidants or reducing agents and can also provide a protective coating. Saving energy owing to the availability and facile synthesis at room temperature and ambient atmosphere is the main advantage of using environmentally benign plant extracts as an antioxidant for the synthesis of nanoparticles [36,37].

In a recent review on nanostructured MnO_2 as electrode material for energy storage, we pointed out that the problems of the Zn/MnO_2 battery (limited cycling life and power) have now been entirely solved. The alkaline Zn/MnO_2 batteries now outperform the Li-ion batteries not only by the lower price, but also by their performance, both in energy and in power density [10]. In particular, Liu et al. reported such a battery, the capacity of which was 285 $mAh \cdot g^{-1}$ (MnO_2), with capacity retention of 92% over 5000 cycles [38]. MnO_2 is thus a promising candidate to be the electrode of next generation of commercial rechargeable batteries. The next problem is thus to optimize the synthesis of this material in terms of cost and environmental friendliness. The present work addresses this problem by employing a facile, eco-friendly and cost-effective method using green and black teas to prepare α-MnO_2.

Black and green teas exhibiting different structures contain number of flavonoids (one of constituents of polyphenols) that can be used as species to prepare MnO_2 from the redox reaction of $KMnO_4$. They have excellent antioxidant properties due to the high phenolic content [39]. Green tea leaves are not fermented and hence, do not go through the oxidation process that black tea undergoes, making it extremely rich in simple flavonoids called epigallactocatechin gallate (the EGCG), a popular antioxidant. The oxidation process used to obtain black tea converts catechins to more complex varieties called theaflavins and thearubigins. Hence, green tea is ahead of black tea in its antioxidant quality and quantity. Fig.

1 summarizes the chemical structures of the major flavonoids found in both green and black tea. The oxidation process modifies only the type of flavonoids present without changing the level and antioxidant activity of these flavonoids [40-43].

The goal of this paper is to synthesize MnO_2 nanoparticles by a simple redox synthesis method using extracts of green and black tea as reducing agents for their use as high-performing electrode materials in energy storage systems. We pay a special attention to characterize the crystal chemistry of α-type MnO_2 prepared from redox reaction of potassium permanganate, which always contains a residual fraction of K^+ ions in the 2×2 tunnels preserving the structural stability of this material. Note that most of numerous works published in the literature neglect this aspect; only few papers consider the presence of potassium in the cryptomelane framework [44-51]. Two samples were prepared using a redox synthesis procedure assisted by biologic anti-oxidant reagents that are extracts of tea. Structural and morphological properties of MDOs are investigated by X-ray diffraction (XRD), thermal gravimetric analysis (TGA), specific surface area, pore volume and mean pore size, Raman scattering (RS) spectroscopy, scanning electron microscopy (SEM), and transmission electronic microscopy (TEM). Further electrochemical tests are also performed by cyclic voltammetry (CV), galvanostatic experiments and electrochemical impedance spectroscopy (EIS). Our results reveal that nanostructured α-MnO_2 particles exhibit both improved specific capacity and high rate capability Note only intrinsic properties of α-MnO_2 are considered here, so that the results are not comparable with the electrochemical properties of the composites above mentioned, since the other elements of the composites are introduced just because they improve the performance.

2. Experimental

2.1. Sample preparation

Two samples of MnO_2 were prepared using a green synthesis method via redox reaction between $KMnO_4$ and extracts of green tea (GT-MnO_2) and black tea (BT-MnO_2). A commercial green tea bag of 1.8 g was boiled in 100 mL distilled water for 5 min to extract the green tea solution. The cooled prepared extract was added drop by drop to 3 g $KMnO_4$ acidified with 2 mL of 2.5 mol L^{-1} H_2SO_4 in 100 mL of distilled water. After stirring

vigorously for 1 h at room temperature, the color of the solution changed from purple to black due to the complete reduction of $KMnO_4$ by the extract of green tea. The black precipitate was isolated by filtration and washed several times with distilled water to remove most of the expected K^+ from the precipitate. The collected precipitate was dried overnight at 90 °C, then calcined at 300 °C for 5 h in ambient atmosphere. The same procedure was used to prepare BT-MnO_2 sample using the extracts of boiled two bags (2 g) of black tea added to 3 g of $KMnO_4$.

2.2. Structural and electrochemical characterization

Thermal gravimetric (TG) measurements were carried out using an analyzer (Perkin Elmer, TGA 7 series) in the temperature range of 50–1000 °C in air at a heating rate of 10 °C min^{-1}. The crystal structure was investigated by X-ray powder diffraction using a STOE STADI-P with Mo-$K_{\alpha 1}$ radiation (λ=0.70932 Å), curved Ge111 monochromator and Si-strip detector from Dectris. Samples were placed in 0.5-mm glass capillaries. Specific surface area, pore volume and mean pore size of the samples were obtained by performing N_2 physisorption experiments at 77 K on Micromeritics ASAP (Tristar 2020, USA) analyzer using Brunauer–Emmett–Teller (BET) and Barrett–Joyner–Halenda (BJH) multipoint methods. The micropore volume (V_{pore}) was calculated from the amount of N_2 adsorbed at a relative pressure ($P_r = P/P_0$) of 0.1 and 0.95, respectively. Raman scattering (RS) spectra were collected on a LabRam Evolution HR (HORIBA) spectrometer equipped with a Nd:YAG laser (523 nm, 1 mW). The final spectrum consists of two independent acquisitions with a total acquisition time of 720 seconds. The morphology and size of particles were investigated by scanning electron microscopy (SEM) (model Quanta FEG 250) and transmission electron microscopy (TEM) (model JEM-2100, JEOL, Japan). Swagelok type cells were used to characterize the materials electrochemically. For this purpose, the active material was mixed with carbon back (Super P, Timcal) in the ratio 8:2. The cathode loading was 4.2 mg cm^2 (geometric surface area 1.8 cm^2). Two layers of Whatman GF/B separators and 1 mol L^{-1} $LiPF_6$ in an ethylene carbonate and dimethyl carbonate solution (1:1) mixture were used for the cell assembly. Lithium metal was used as counter electrode. The material was characterized galvanostatically using the LICCY cycling station (Lithium Cell Cycler Liccy, KIT). VMP3 potentiostat (Biologic Science Instruments, France) was used to record the cyclic voltammograms (CV). Electrochemical

impedance spectroscopy (EIS) was carried using a phase sensitive multimeter (model PSM 1700, UK) in the frequency range 0.01 Hz–100 kHz using a voltage bias of 5 mV.

3. Results and discussion

3.1. Elemental and structural studies

The cryptomelane (α-MnO_2) phase commonly prepared via redox reaction of $KMnO_4$ or $K_2Mn_2O_8$ contains potassium as an essential constituent filling the 2×2 tunnels. Potassium ions are incorporated during the synthesis because of the excess of K^+ ions in the solution. α-MnO_2 crystallizes in the body-centered tetragonal structure with *I*4/*m* space group; the unit cell contains 16 oxygen sites, 8 sixfold coordinated ^{VI}Mn sites, and 2 eightfold coordinated tunnel sites (^{VIII}K). Consequently, the formula of the α-phase is $K_xMn_8O_{16}$, in which the concentration of K^+ ions is variable, but K never occupies more than 50% on any of the sites in the lattice [38]. This concentration can be determined from thermogravimetry (TG) by analyzing the weight loss of chemisorbed water in the tunnels and the decomposition temperature from MnO_2 to Mn_2O_3 (Fig. 2). Poyraz et al. [46] reported that the $K_xMn_8O_{16}$ samples with low K^+ content, $K_{0.32}Mn_8O_{16}$, have a lower decomposition temperature of 510 °C compared to *T*=580 °C for the samples with high K^+ content ($K_{0.75}Mn_8O_{16}$). Fig. 2a shows the differential (DTG) weight loss for GT-MnO_2 and BT-MnO_2 synthesized by redox reaction between $KMnO_4$ and extracts of green tea and black tea, respectively. The decomposition of α-K_xMnO_2 to Mn_2O_3 operates via an exothermic reaction that takes place at temperatures 500<*T*<650 °C. Distinct weight losses caused by the reduction of tetravalent Mn^{4+} ions to trivalent Mn^{3+} ions correspond to oxygen evolution $2MnO_2 \rightarrow Mn_2O_3 + ½O_2$ that is completed at *T*~650 °C [49]. Using previous DTG analyses, an almost linear relationship (*R*=0.984) between the temperature of the MnO_2 to Mn_2O_3 phase transition and the concentration of K^+ ions in the 2×2 tunnels (Fig. 2b) was established. Data summarized in Table 1 show that the BT-MnO_2 has a lower concentration of K^+ ions (only about half the value) than GT-MnO_2.Fig. 3 shows the XRD patterns for GT-MnO_2 and BT-MnO_2 samples. All the reflections can be indexed with the α-MnO_2 structure (JCPDS 44-0141). The X-ray diagram of GT-MnO_2 has the feature of nanostructured material with broadening of Bragg reflections (curve a), while curve (b) shows that BT-MnO_2 is an amorphous or highly disordered material. Scherrer crystallite sizes of

8.0±0.2 nm for the GT-MnO_2 sample and 4.4±0.2 nm for the BT-MnO_2 sample were calculated from the half-width of the <211> reflection at 2θ=37.6° (with Scherrer parameter K=0.88). A Rietveld refinement for GT-MnO_2 using the program package Fullprof [52] confirms nanosized needles along the *c*-axis. Refinement parameters are R_p=16.7; R_{wp}=18.6; R_{exp}=14.05; χ^2=1.75 and Bragg R-factor=5.8. As suggested by Vicat et al. [45] the structure is described with an interstitial potassium site on Wyckoff position 4*e* (0,0,*z*) in addition to the 8*h* sites for Mn, O1, O2, with *z*~0.3. The occupancy of this site is approximately 0.068/0.25 = 27%; the other sites are fully occupied and the *z*-coordinate converges at 0.35. This leads to a potassium content of 0.135 per formula unit, consistent with the value of 0.11(2) from the TG measurements. The formula of $K_{0.135}MnO_2$ leads to an average oxidation state +3.865 for Mn ions, in which the number of $^{VI}Mn^{3+}$ is equal to the number of $^{VIII}K^+$. Lattice parameters listed in Table 2 are in good agreement with reported values [53]. Besides the scale and background points, the refined parameters were isotropic atomic displacement parameter (ADP), lattice parameter, atomic positions and two parameters for anisotropic size broadening. Note that the ratio K:Mn = 0.135 is very close to the value for cryptomelane structure $K_{0.125}MnO_2$ (KMn_8O_{16}) with half occupancy of the 4*e* tunnel sites.

Note that very fast preparation of the GT-MnO_2 sample, did not allow a complete removal of K^+ ions, despite several washings with distilled water. Consequently, a higher number of alkali ions was trapped in comparison with BT-MnO_2, which was formed slowly. The synthesis process is affected by the strength of the reducing agent, which governs the ionic extraction from the 2×2 cavities and controls the diffusion of K^+ ions. As an experimental result, the redox reaction assisted by black tea is not as fast as with green tea, because of the difference in the flavonoid structure and the strength of the antioxidant species.

Fig. 4 presents the SEM and TEM images of GT-MnO_2 and BT-MnO_2. Submicron-sized particles with average size ~400 nm have almost identical shape and distribution for both samples. These secondary particles are composed of interconnected nanoneedles with diameter of 5 nm and length of ~100 nm as shown in the TEM pictures. Note that the shape and size of both the agglomerates and the nanoneedles of GT- and BT-MnO_2 are similar.

The pore characteristics, i.e. BET surface area, pore volume and mean pore size, are shown in Table 3. The value S_{BET} of 49.8 m^2 g^{-1} for GT-MnO_2 can be compared with 9.37 m^2 g^{-1} for

α-MnO_2 synthesized via hydrothermal treatment of a precursor γ-MnO_2 [54] and S_{BET}=41 m^2 g^{-1} for γ-MnO_2 synthesized by Pechini technique [55].

Raman scattering (RS) spectra of GT-MnO_2 and BT-MnO_2 nanoneedles are displayed in Fig. 5. As Raman spectroscopy is a powerful tool for the analysis of the structure at the molecular scale, this technique was used to study the crystallinity of the manganese dioxide depending on the synthesis procedure, i.e. the nature of the reducing agents. The RS spectrum of GT-MnO_2 exhibits well-resolved bands at 181, 380, 510, 577, 630 and 754 cm^{-1}, while the Raman bands of BT-MnO_2 are broadened and poorly resolved, which is the fingerprint of a highly disordered material. Note that the Raman features of our polycrystalline samples do not allow the observation of all active modes ($6A_g+6B_g+3E_g$) predicted by the group factor analysis of the body-centered tetragonal structure [56]. The two high-frequency bands at 577 and 630 cm^{-1} (A_g modes), which originate from breathing Mn-O vibrations perpendicular to the direction of double chains of edge-shared [MnO_6] octahedra, are the typical fingerprints of the tetragonal 2×2 tunnel structure. The low-frequency Raman band at 181 cm^{-1} assigned to an external vibration comes from translational motion of the [MnO_6], while the band at 380 cm^{-1} is attributed to the O-Mn-O bending vibrations. The shoulder at 754 cm^{-1} is related to the antisymmetric Mn-O stretching vibrations. These outlined Raman features are in good agreement with results reported in the literature for α-MnO_2 [57,58]. Note that the degree of crystallinity of synthesized MnO_2 samples has a strong impact on the intensity of the ν_{577} and ν_{630} bands. In summary, Raman data match well with results from XRD showing that GT-MnO_2 has a better crystallinity than BT-MnO_2.

3.2. Electrochemical behavior

Electrochemical properties and discharge performance of MnO_2 nanoparticles synthesized by the green synthesis assisted by extracts of tea were investigated by cyclic voltammetry, galvanostatic charge-discharge experiments, and cycling tests at different current densities from 10 to 400 mA g^{-1} (1C=260 mA g^{-1}). Fig. 6 shows the first 20 cyclic voltammograms carried out at scan rate of 0.1 mV s^{-1} in the potential range 1.5-3.5 V vs. Li^+/Li^0. The first discharge-charge process is unique with features dominated by the broad cathodic peaks $V_{c,1}$ at 2.45 and 2.40 V for GT-MnO_2 and BT-MnO_2 electrodes, respectively, and the corresponding oxidation peaks observed at 3.10 and 2.40 V. The broadness is attributed to the poor

crystallinity rather than the morphology of nanoneedles. Such behavior has been reported several times [48,59-61]. It was conjectured that local activation can take place in the material during the initial lithium insertion. Dai et al. [59] believed that the change of the initial charge-discharge curves is due to ion-exchanged reaction. Zhang et al. [61] studied the chemical states of the species in K_xMnO_2 using X-ray photoelectron spectroscopy (XPS) and concluded that potassium is extracted from the host lattice, which described the CV profile evolution during the first cycle. The electrochemical reactions of the second cycle show different profiles with two pronounced sets of redox peaks. Values of the redox potentials are listed in Table 4. Note that the difference between V_{red} and V_{oxid} is ΔV=~0.15 V irrespective of the degree of structural order. The subsequent cycles have almost the same profile, so that the lithium insertion/extraction process occurs most probably with the same mechanism. In the forthcoming cycles these CV data show a good rechargeability for both samples, so that a good structural stabilization is obtained after the second cycle. The initial broad cathodic peak seems to be dependent on the K^+ content in α-K_xMnO_2; the higher the K^+ content the higher the cathodic potential [49,59-61]. This is consistent with the assumption that Li^+ motion requires a stable tunnel framework, which is ensured by the presence of larger cations such as K^+. It is well known that Li^+ ions are located on off-center 8*h* and 8*h*' Wyckoff positions (near the walls of the 2×2 tunnels) and the presence of K^+ ions on the centered 4*e* sites affects the electrochemical features and the overall discharge capacity [45].

Fig. 7 illustrates the available sites of the cryptomelane structure occupied by Li^+ and K^+ cations. The initial electrochemical modification is attributable to the lithium-cell formation, plus the structural evolution that results from the so-called "loss of lithium inventory" [62]. This loss is due to the trapping of a small amount of Li^+ ions inserted during the first discharge and remaining in the tunnel structure, which results in stabilization of the tetragonal phase. This behavior is consistent with the two pseudo-plateaus observed in the discharge profiles (see Fig. 8). Similar results have been observed previously [63,64]. Johnson et al. [63] reported the immediate appearance of two sets of redox peaks in α-MnO_2 prepared by the reaction between Mn_2O_3 and H_2SO_4. The evolution of the cyclic voltammogram was observed in the case of a silicon anode for which the authors claim a local activation taking place during the initial lithiation for very small nanocrystallites, i.e. L<10 nm [64]. In the present study, the morphology of nanoneedles of 5 nm diameter favors the insertion of Li^+ ions on the two

different 8*h* and 8*h*' Wyckoff sites of the $Li_xK_{0.135}MnO_2$ structure; the first set of redox peaks correspond to the lithiation of 8*h* position at low Li concentration, while the second set is due to the 8*h*' site occupation for high Li content that requires different energies of formation [65]. To the contrary, Zhang et al. [61] reported a strong cathodic peak at ~2.2 V during the first cycle, which shifted toward higher potential for the second and further cycles, showing that lithium insertion-extraction in/from cryptomelane-type $K_{0.25}Mn_2O_4$ occurred as a single set of redox reaction at 2.5/3.0 V because the sample in their work consisted of microspheres composed of nanofibers in the range of 10-20 nm diameter.

Fig. 8 shows the discharge-charge profiles of MnO_2//Li cells recorded at constant current density 10 mA g^{-1} (C/26) in the potential range 1.5–3.5 V vs. Li^+/Li^0 including GT-MnO_2 and BT-MnO_2 as positive electrode materials. In the entire discharge range, the discharge cell potential decreases slowly and evidences the presence of two pseudo-plateaus; each of them appears as an "S-shaped" curve, which indicates a topotactic reaction for the lithium insertion in both electrodes. However, the voltage decay is more pronounced in BT-MnO_2, which is characteristic of a disordered electrode material [1]. These features are thus consistent with the structural analysis.

The net effect of the presence of K^+ ions in 2×2 tunnels (located on 4*e* Wyckoff positions) is observed in the discharge curves. The initial specific capacity of highly disordered BT-MnO_2 is ~236 mAh g^{-1}, while the well crystallized GT-MnO_2 delivers ~198 mAh g^{-1}. The lower initial capacity is attributed to the presence of the higher concentration of electrochemically inactive K^+ ions trapped on 4*e* sites inside the large tunnel (4.6 Å). In GT-MnO_2, more than half of the 4*e* sites are occupied by potassium, against only one quarter in BT-MnO_2. This inactive cation may hinder the Li insertion into the tunnel and impede the diffusion during the discharge process [25]. The structural stabilization of K^+ cation is clearly evidenced in the GT-MnO_2 structure, for which the capacity fading is lower than for BT-MnO_2 (Fig. 9). Note that a similar capacity loss for Li//α-MnO_2 cells was reported in several works [28, 66-68]. The Faraday yield of 0.7 F/mole for GT-MnO_2 is consistent with the mean oxidation state +3.865 for Mn ions determined form the Rietveld refinement. Except for the two first cycles, the coulombic efficiency on the third and subsequent cycles for GT-MnO_2 shows good rechargeability with efficiency close to 99% even at constant current density of 200 mA g^{-1} (≈0.75C).

The cycling performance, i.e. discharge capacity and coulombic efficiency over 54 cycles, of cells with K_xMnO_2 as cathodes is shown in Fig. 9. The GT-MnO_2 sample shows the best results for capacity retention. The relevant coulombic efficiency of the $K_{0.135}MnO_2$ electrode remains around 100% after several cycles, indicating the good reversibility. At C/26 rate, the specific discharge capacity of GT-K_xMnO_2 decreases slowly from 161 mAh g^{-1} (3^{rd} cycle) to 141 mAh g^{-1} (54^{th} cycle). The capacity loss rate is 0.25% and 0.58% per cycle for GT-K_xMnO_2 and BT-K_xMnO_2, respectively. Both samples suffer from an irreversible capacity in the first cycle, but it is a limited loss of ~30 mAh g^{-1} for GT-MnO_2 so that GT-MnO_2 retains 73% from its initial capacity at the 20^{th} cycle, whereas BT-MnO_2 retains only 62%. The first cycle irreversible capacity (1^{st} IC) is an intrinsic weakness of MDOs. Several examples are obtained in the literature. The 1^{st} IC of 85 mAh g^{-1} was reported for birnessite MnO_2 nanobelts [66], Huang et al. [67] indicated a 1^{st} IC of 75 mAh g^{-1} for macroporous β-MnO_2 and Cheng et al. [66] reported a 1^{st} IC larger than 40 mAh g^{-1} for α-MnO_2 nanowires. Covering α-MnO_2 nanorods by a thin layer of carbon improves the long-term capacity retention, but does not inhibit the initial capacity loss that confirms the trapping of a fraction of lithium ions into the internal cavities during the cell formation [27]. Yang et al. [69] showed that hydrothermally synthesized α-MnO_2 composed of nanorods ~20 nm diameter delivers specific capacity of 189 mAh g^{-1} at a discharge current 50 mA g^{-1}.

Rate performance was tested for both samples at various current densities in the range 10-400 mA g^{-1} (1C=260 mA g^{-1}). Figs. 10a and 10b show the rate capabilities and the modified Peukert plot, respectively. As for many electrodes, the decay of the discharge capacity follows a semi-logarithmic law with increase of the current passed through the cell. After the tests at higher C-rates up to 1.5C, the capacity delivered at the initial current density of 10 mA g^{-1} was recovered, which gives evidence of the electrochemical reversibility and structural stability of the samples. A reversible capacity of 32 mAh g^{-1} was delivered for the Li//GT-MnO_2 cell cycled at 1.5C, while that of the Li//BT-MnO_2 vanished due to the sluggish kinetics of Li^+ ions associated with the structure.

Fig. 11 shows the electrochemical impedance spectra (EIS) of MnO_2 electrodes over the frequency range 0.01 Hz-100 kHz as a function of the cell potential: 3.0 V and 1.8 V vs. Li^+/Li^0 corresponding to the lithium insertion $x \approx 0.05$ and ≈ 0.6 in Li_xMnO_2, respectively. All EIS features are composed in the high-frequency region of a semi-circle that reveals the

electrolyte resistance R_s and the charge transfer resistance R_{ct} and inclined lines in the low-frequency range attributed to the Warburg impedance σ_w and the electrode capacitance. The Warburg regime observed at low frequencies gives evidence that the insertion mechanism of Li^+ ions into the MnO_2 electrode is strongly controlled by a diffusion process. In this regime, the impedance varies with the angular frequency ω according to the law [70]:

$$Z' = R_s + R_{ct} + \sigma_w \omega^{-1/2}, \quad (1)$$

The Warburg impedance σ_w is obtained from the slope of Z' vs. $\omega^{-1/2}$ in the low-frequency range (Fig. 11). Typical values of σ_w are listed in Table 5. EIS can be used to evaluate the apparent Li-ion diffusion coefficient D_{Li+} from the low-frequency Warburg impedance according the relation [71]:

$$D_{Li^+} = \frac{1}{2}\left[\frac{RT}{F^2 A C_{Li} \sigma_W}\right]^2, \quad (2)$$

where R, T and F are the usual constants, A the surface area of the electrode-electrolyte interface, C_{Li} is the lithium-ion concentration in the electrode. Note that estimation of A is rather difficult. Instead of the apparent geometric surface area of the electrode (1.8 cm^2), we have used the S_{BET} values that take into account the porosity of the electrodes. Randles parameters and diffusion coefficient D_{Li+} are reported in Table 5.

3.3. Discussion

The cryptomelane α-MnO_2 tunnel-based structure include well-aligned 2×2 (4.6×4.6 $Å^2$) tunnels occupied with large K^+ cations and empty 1×1 (1.9×1.9 $Å^2$) tunnels intergrowth along the *c* axis. α-MnO_2 is believed to show topotactic reduction of Mn (Li^+ solid solution) during lithiation [48]. The role of large cations (K^+) occupying the central 2*a* site of 2×2 tunnels is considered as follows. The presence of large tunnel counter cations in the MnO_2 lattice is a necessary condition for the growth of the hollandite-type MnO_2 (HMDO) structure and prevents the formation of other MnO_2 polymorphs [53]. Generally, the presence of K^+ ions in the (2×2) tunnels of the hollandite lattice has an impeding effect for the chemical diffusion of

the Li^+ ions. This is due to the much bigger ionic radius of K^+ (r_i=1.33 Å) than Li^+ (r_i=0.69 Å), which prevents the facile lithium motion in the MnO_2 framework [72]. The stabilizing K^+ ions only partially occupy the space inside structural tunnels of cryptomelane $K_xMn_8O_{16}$, leaving enough volume for Li^+ ion insertion, leading to superior discharge rate performance compared to the ones of pristine α-MnO_2 material. Byles et al. [73] evaluated the electronic and ionic conductivities of tunnel structured MnO_2 and shown the stabilization of K^+ and Mg^{2+} cations in cryptomelane and todorokite frameworks. Our EIS data show that the charge transfer resistance is a function of the K^+ content: R_{ct}=83.2 Ω for $K_{0.135}MnO_2$ increases to 105.8 Ω for $K_{0.06}MnO_2$. The role of tunnel cation on electrochemical performance of cryptomelane type α–MnO_2 ($K_xMn_8O_{16}$) cathode materials with tunable K^+ content has been investigated by Poyraz et al. [46]. The electrochemistry of the $K_xMn_8O_{16}$ electrode with varying K/Mn ratios (0.000 to 0.094) was evaluated. For x=0.32, the α-MnO_2 electrode showed higher voltage, higher specific energies, and improved capacity retention compared to the material with x=0.75. Another effect of the interstitial K^+ cation incorporation in the α-MnO_2 lattice is the formation of newly occupied electronic states that appear inside the original MnO_2 bandgap, indicating mixed Mn^{4+} and Mn^{3+} in K_xMnO_2 [74]. This indicates that the presence of K^+ inside the 2×2 tunnels can enhance the electronic conductivity of α-MnO_2 through electron hopping between heterovalent Mn pairs (Mn^{4+}/Mn^{3+}). It was found from EIS data that the presence of K^+ inside the 2×2 tunnels of α-MnO_2 nanoneedles improves both their electronic conductivity and Li^+ diffusivity. These enhancements facilitate favorable electrode kinetics, and thus result in good rate performance of Li/α-MnO_2 based batteries.

Compared with other nanoscale-sized lithiated MnO_2 cathodes reported previously, the present α-MnO_2 powders exhibit similar trends in kinetics [49,75-79]. The lithium diffusion coefficient 3.4×10^{-14} m^2 s^{-1} at 20 °C in electrolytic $Li_{1.0}MnO_2$ (battery grade γ-phase) was early determined by galvanostatic technique [75]. Using cyclic voltammetry, Bach et al. [76] estimated a diffusion coefficient of Li^+ ions of $\approx10^{-10}$ cm^2 s^{-1} in the hydrated a-phase $K_{0.062}MnO_2$. Current step method was used to measure the Li chemical diffusion coefficient of $D_{Li}=4\times10^{-11}$ cm^2 s^{-1} in $Li_{0.4}MnO_2$ [75]. D_{Li^+} values were found to vary in the range from 1×10^{-10} cm^2 s^{-1} for the fully charge (delithiated) state to 2×10^{-11} cm^2 s^{-1} for the fully discharged (lithiated) state [78,79]. Yuan et al. [49] show that after K^+ removal the charge transfer

resistance (R_{ct}) increases and the diffusion coefficient D_{Li+} decreases from 1.91×10^{-12} cm^2 s^{-1} in $K_{0.25}MnO_2$ to 7.16×10^{-13} cm^2 s^{-1} in $K_{(0.25-x)}MnO_2$. Our results are consistent with those of previous reports. We show that kinetics for Li^+ ions is a function of the concentration of K^+ cations into the tunnels; diffusion coefficient D_{Li} in $K_{0.06}MnO_2$ is lower than that in $K_{0.135}MnO_2$, which is consistent with $D_{Li}=1.9\times10^{-12}$ cm^2 s^{-1} for $K_{0.25}MnO_2$ reported by Yuan et al. [49]. From electrochemical impedance spectroscopy (EIS), we have shown the effect of K^+ on the ionic transport of lithium inserted into the α-K_xMnO_2 lattice and on the electronic conduction.

4. Conclusions

A green synthesis route involving the redox reaction between $KMnO_4$ and antioxidant reagent was used to obtain nanosized α-MnO_2. Cheap and benign biological reducing reagents were obtained from extracts of green tea and black tea. In both cases, the samples were obtained in the form of particles with ~400 nm in size, composed of interconnected needles with diameter of 5 nm and length of ~100 nm. Further characterization by thermal gravimetric analysis and Raman scattering emphasized different structural properties for the two samples, related to the different antioxidant reagents in the green and black tea. These samples synthesized by using biological reducing agents showed electrochemical performance comparable with that of samples prepared by conventional more expensive methods using chemical reducing agents. The sample synthesized using black tea showed better initial capacity (~231 mAh g^{-1}) than the sample synthesized using green tea GT-MnO_2 (~214 mAh g^{-1}). However, GT-MnO_2 shows better capacity retention (73% after 20 cycles at current density 10 mA g^{-1}) than BT-MnO_2 (62% at the same cycle number). GT-MnO_2 also showed improved rate capabilities compared to BT-MnO_2. This cheaper and scalable redox synthesis process is thus a significant improvement with respect to the industrial processes currently used to fabricate the commercialized MnO_2 batteries. The chemical diffusion coefficient of Li^+ ions inserted in Li_xMnO_2 frameworks was determined from EIS experiments as a function of the discharge state that show higher kinetics for Li^+ transport in $K_{0.06}MnO_2$ compared with $K_{0.135}MnO_2$.

References

[1] C.M. Julien, A. Mauger, A. Vijh, K. Zaghib, Lithium batteries: science and technology, Springer, Heidelberg, 2016, pp. 1-27.

[2] K. Wen, G. Chen, F. Jiang, X. Zhou, J. Yang, A facile approach for preparing MnO_2-graphene composite as anode material for lithium-ion batteries, Int. J. Electrochem. Sci. 10 (2015) 3859-3866

[3] H. Huang, X. Wang, Design and synthesis of Pd-MnO_2 nanolamella-graphene composite as a high-performance multifunctional electrocatalyst towards formic acid and methanol oxidation. Phys. Chem. Chem. Phys. 15 (2013) 10367-10375.

[4] Y. Su, S. Li, D. Wu, F. Zhang, H. Liang, P. Gao, C. Cheng, X. Feng, Two-dimensional carbon-coated graphene/metal oxide hybrids for enhanced lithium storage. ACS Nano 6 (2012) 8349-8356.

[5] V. Etacheri, R. Marom, R. Elazari, G. Salitra, D. Aurbach, Challenges in the development of advanced Li-ion batteries: a review. Energy Environ. Sci. 4 (2011) 3243-3262.

[6] L. Li, A.O. Raji, J.M. Tour, Graphene-wrapped MnO_2-graphene nanoribbons as anode materials for high-performance lithium ion batteries. Adv. Mater. 25 (2013) 6298-630.

[7] W. Yong, D. Panshuang, W. Chao, Fabrication and lithium storage properties of MnO_2 hierarchical hollow cubes. J. Alloys Compd. 654 (2016) 273-279.

[8] F. N. I. Sari, P.-R. So, J. M. Ting, MnO_2 with controlled phase for use in supercapacitors. J. Am. Ceram. Soc. 100 (2017) 1642-1652.

[9] L. Athouel, P. Arcidiacono, C. Ramirez-Castro, O. Crosnier, C. Hamel, Y. Dandeville, P. Guillemet, Y. Scudeller, D. Guay, D. Bélanger, T. Brousse, Investigation of cavity microelectrode technique for electrochemical study with manganese dioxides. Electrochim. Acta 86 (2012) 268-276.

[10] C.M. Julien, A. Mauger, Nanostructured MnO_2 as electrode materials for energy storage. Nanomaterials 7 (2017) 396.

[11] Y. Su, J. Zhang, K. Liu, Z. Huang, X. Ren, C.-A. Wang, Simple synthesis of a double-shell hollow structured MnO_2@TiO_2 composite as an anode material for lithium ion batteries. RSC Adv. 7 (2017) 46263.

[12] C. Liu, Tao Peng, C. Wang, Y. Lu, H. Yan, Y. Luo, Three-dimensional $ZnFe_2O_4$@MnO_2 hierarchical core/shell nanosheet arrays as high-performance battery-type electrode materials. J. Alloys Compd. 720 (2017) 86-94.

[13] G. Yang, S.-J. Park, MnO_2 and biomass-derived 3D porous carbon composites electrodes for high performance supercapacitor applications. J. Alloys Compd. 741 (2018) 360-367.

[14] S. Palanisamy, P. Periasamy, K. Subramani, A. Prabhakaran Shyma, R. Venkatachalam, Ultrathin sheet structure Ni-MoS_2 anode and MnO_2/water dispersion graphene cathode for modern asymmetrical coin cell supercapacitor. J. Alloys Compd. 731 (2018) 936-944.

[15] N. Zhang, Y. Ding, J. Zhang, B. Fu, X. Zhang, X. Zheng, Y. Fang, Construction of MnO_2 nanowires@$Ni_{1-x}Co_xO_y$ nanoflake core-shell heterostructure for high performance supercapacitor. J. Alloys Compd. 694 (2017) 1302-1308.

[16] X. Cui, X. Chen, W. Zhang, X. Yan, M. Wang, J. Lian, Z. Zheng, H. Deng, Developing a facile method to construct 3D hierarchical $CoMoO_4$@C@MnO_2 core-shell structure aligned on Ni foam with enhanced pseudocapacitive performances. J. Alloys Compd. 695 (2017) 2109-2116.

[17] Y. Zhang, T. Mao, L. Cheng, H. Wu, R. Wu, L. Zheng Tunable morphology and property of a MnO_2/carbonized cotton textile hybrid electrode for electrochemical capacitors. J. Alloys Compd. 729 (2017) 655-662.

[18] J. Zhang, Y. Li, Y. Zhang, X. Qian, R. Niu, R. Hu, X. Zhu, X. Wang, J. Zhu, The enhanced adhesion between overlong TiN_xO_y/MnO_2 nanoarrays and Ti substrate: Towards flexible supercapacitors with high energy density and long service life. Nano Energy 43 (2018) 91-102.

[19] F. N. S. Xi, Y. Zhu, Y. Yang, Y. Liu, Direct synthesis of MnO_2 nanorods on carbon cloth as flexible supercapacitor electrode. J. Nanomat. 2017 (2017) 7340961.

[20] X. Lv, H. Zhang, F. Wang, Z. Hu, Y. Zhang, L. L. Zhang, R. Xie, J. Ji, Controllable synthesis of MnO_2 nanostructure anchored on graphite foam with different morphology for high-performance asymmetric supercapacitor. Cryst.EngComm (2018) DOI: 10.1039/C7CE02108A (in press)

[21] Y. Wang, P.-S. Ding, M.-G. Zou, W.-B. Guo, D.-X. Wang, F.-C. Zhang, Synthesis of nanosheet-based MnO_2 hollow capsules and their application in lithium batteries. Ferroelectrics 522 (2018) 75-79.

[22] M. H. Ghorbani, A. M. Davarpanah, Synthesis and characterization of MnO_2 nanowires. Modern Phys. Lett. B 31 (2017) 1750006.

[23] X. Bai, W. Zhu, W. Yao, T. Duan, Hydrothermal preparation of CS@MnO_2 with different morphologies for supercapacitor electrode materials. Mater. Lett. 210 (2018) 329-332.

[24] S. Birgisson, D. Saha, B. B. Iversen, Formation mechanisms of nanocrystalline MnO_2 polymorphs under hydrothermal conditions. Cryst. Growth Des. 18 (2018) 827–838.

[25] N. Zhang, L. Li, J. Zhao, T. Yang, G. Zhang, H. He, S. Sun, Precisely controlled synthesis of α-/β-MnO_2 materials by adding $Zn(acac)_2$ as a phase transformation-inducing agent. Chem. Commun. 54 (2018) 1477-1480.

[26] J. Yao, Q. Pan, S. Yao, L. Duan, J. Liu, Mesoporous MnO_2 nanosphere/graphene sheets as electrodes for supercapacitor synthesized by a simple and inexpensive reflux reaction. Electrochim. Acta 238 (2017) 30-35.

[27] R. Mohan, R. Paulose, V. Parihar, Hybrid MnO_2/CNT nanocomposite sheet with enhanced electrochemical performance via surfactant-free wet chemical route. Ionics 23 (2017) 3245-3248.

[28] J. Milne, I. Zhitomirsky, Application of octanohydroxamic acid for liquid-liquid extraction of manganese oxides and fabrication of supercapacitor electrodes. J. Colloid Interface Sci. 515 (2018) 50-57.

[29] P. Xia, B. Zhu, B. Cheng, J. Yu, J. Xu, 2D/2D g-C_3N_4/MnO_2 Nanocomposite as a direct Z-scheme photocatalyst for enhanced photocatalytic activity. ACS sustainable Chem. Eng. 6 (2018) 965-973.

[30] A.M. Hashem, H.M. Abuzeid, D. Mikhailova, H. Ehrenberg, A. Mauger, C.M. Julien, Structural and electrochemical properties of α-MnO_2 doped with cobalt. J. Mater. Sci. 47 (2012) 2479-2485.

[31] A.M. Hashem, H.M. Abuzeid, A.E. Abdel-Ghany, A. Mauger, K. Zaghib, C.M. Julien, SnO_2-MnO_2 composite powders and their electrochemical properties. J. Power Sources 202 (2012) 291-298.

[32] A.M. Hashem, H. Abuzeid, A. Abdel-Latif, H. Abbas, H. Ehrenberg, S. Indris, A. Mauger, C.M. Julien, MnO_2 Nano-rods prepared by redox reaction as cathodes in lithium batteries. ECS Trans. 50(24) (2013) 125-130.

[33] P. Kanha, P. Saengkwamsawang, Effect of stirring time on morphology and crystalline features of MnO_2 nanoparticles synthesized by co-precipitation method. Inorg. Nano-Metal Chem. 47(8) (2017) 1129-1133.

[34] A. Khan, H. Wang, Y. Liu, A. Jawad, J. Ifthikar, Z. Liao, T. Wang, Z. Chen, Highly efficient α-Mn_2O_3@α-MnO_2-500 nanocomposite for peroxymonosulfate activation: comprehensive investigation of manganese oxides. J. Mat. Chem. A 6 (2018) 1590-1600.

[35] C. A. Romano, M. Zhou, Y. Song, V. H. Wysocki, A. C. Dohnalkova, L. Kovarik, L. Pasa-Tolic, B. M. Tebo, Biogenic manganese oxide nanoparticle formation by a multimeric multicopper oxidase Mnx. Nature Commun. 8 (2017) 746.

[36] S. Yallappa, J. Manjanna, B.L. Dhananjaya, Phytosynthesis of stable Au, Ag and Au–Ag alloy nanoparticles using J. sambac leaves extract, and their enhanced antimicrobial activity in presence of organic antimicrobials. Spectrochim. Acta A 137 (2015) 236-243.

[37] M. Meena-Kumari, J. Jacob, D. Philip, Green synthesis and applications of Au–Ag bimetallic nanoparticles. Spectrochim. Acta A 137 (2015) 185-192.

[38] H. Pan, Y. Shao, P. Yan, Y. Cheng, K.S. Han, Z. Nie, C. Wang, J. Yang, X. Li, P. Bhattacharya, K.T. Mueller, J. Liu, Reversible aqueous zinc/manganese oxide energy storage from conversion reaction. Nat. Energy 1 (2016) 16039.

[39] K. Roy, C.K. Sarkar, C.K. Ghosh, Green synthesis of silver nanoparticles using fruit extract of malus domistica and study of its antimicrobial activity and biostructures. Digest J. Nanomater. 9 (2014) 1137-1147.

[40] F. Cataldo, Green synthesis of silver nanoparticles by the action of black or green tea infusion on silver ions. Eur. Chem. Bull. 3 (2014) 280-289.

[41] M. L. Garcia. B. Pontes, E. E. Nishi, F. K. Ibuki, V. Oliveira, A. C. Sawaya, P. O. Cravalho, F. N. Nogueira, M. D. Franco, R. R. Campos, L. M. Oyama, C. T. Bergamaschi, The antioxidant effects of green tea reduce blood pressure and sympathoexcitation in an experimental model of hypertension. J. Hypertens. 35(2) (2017) 348-354.

[42] Z. Huyut, S. Beydemir, I. Gülçin, Antioxidant and antiradical properties of selected flavonoids and phenolic compounds. Biochem. Res. Int. 2017 (2017) 7616791.

[43] W. Luczaj, E. Skrzydlewska E. Antioxidative properties of black tea. Prev. Med. 40 (2005) 910-918.

[44] R.M. McKenzie, The synthesis of birnessite, cryptomelane, and some other oxides and hydroxides of manganese. Mineral. Mag. 38 (1971) 493-502.

[45] S. Rong, K. Li, P. Zhang, F. Liu, J. Zhang, Potassium associated manganese vacancy in birnessite-type manganese dioxide for airborne formaldehyde oxidation. Catal. Sci. Technol. (2018) DOI: 10.1039/C7CY02121F (in press).

[46] A.S. Poyraz, J. Huang, C.J. Pelliccione, X. Tong, S. Cheng, L. Wu, Y. Zhu, A.C. Marschilok, K.J. Takeuchi, E.S. Takeuchi, Synthesis of cryptomelane type α-MnO_2 ($K_xMn_8O_{16}$) cathode materials with tunable K^+ content: the role of tunnel cation concentration on electrochemistry. J. Mater. Chem. A 5 (2017) 16914-16928.

[47] Y. Yuan, A. Nie, G. M. Odegard, R. Xu, D. Zhou, S. Santhanagopalan, K. He, H. Asayesh-Ardakani, D. D. Meng, R. F. Kile, C. Johnson, J. Lu, R. Shahbazian-Yassar, Asynchronous crystal cell expansion during lithiation of K^+-stabilized α-MnO_2. Nano Lett. 15 (2015) 2998-3007.

[48] Y. Yuan, A. Nie, G.M. Odegard, R. Xu, D. Zhou, S. Santhanagopalan, K. He, H. Asayesh-Ardakani, D.D. Meng, R.F. Klie, C. Johnson, J. Lu, R. Shahbazian-Yassar, Asynchronous crystal cell expansion during lithiation of K^+-stabilized a-MnO_2. Nano Lett. 15 (2015) 2998-3007.

[49] Y. Yuan, C. Zhan, K. He, H. Chen, W. Yao, S. Sharifi-Asl, B. Song, Z. Yang, A. Nie, X. Luo, H. Wang, S.M. Wood, K. Amine, M.S. Islam, J. Lu, R. Shahbazian-Yassar, The influence of large cations on the electrochemical properties of tunnel-structured metal oxides. Nat. Commun. 7 (2016) 13374.

[50] T. Barudzija, N. Cvjeticanin, D. Bajuk-Bogdanovic, M. Mojovic, M. Mitric, Vibrational and electron paramagnetic resonance spectroscopic studies of β-MnO_2 and α-K_xMnO_2 nanorods. J. Alloys Compd. 728 (2017) 259-270.

[51] L. Li, Y. Pan, L. Chen, G. Li, One-dimensional α-MnO_2 trapping chemistry of tunnel structures, structural stability and magnetic transitions. J. Solid State Chem. 180 (2007) 2896-2904.

[52] J. Rodriguez-Carjaval, An introduction to the FullProf program 2000. https://www.psi.ch/sinq/dmc/ManualsEN/fullprof.pdf. Online July 2001.

[53] A. Bystrom, M. Bystrom, The crystal structure of hollandite, the related manganese oxide minerals, and α-MnO_2. Acta Cryst. 3 (1950) 146-154.

[54] V.-P. Dinh, N.-C. Le, T.-P.-T. Nguyen, N.-T. Nguyen, Synthesis of α-MnO_2 nanomaterial from a precursor α-MnO_2: characterization and comparative adsorption of Pb(II) and Fe(III). J. Chem. 2016 (2016) 8285717.

[55] T. Brousse, M. Toupin, R. Dugas, L. Athouël, O. Crosnier, D. Bélanger, Crystalline MnO_2 as possible alternatives to amorphous compounds in electrochemical supercapacitors. J. Electrochem. Soc. 153 (2006) A2171-A2180.

[56] T. Gao, M. Glerup, F. Krumeich, R. Nesper, H. Fjellvag, P. Norby, Microstructures and spectroscopic properties of cryptomelane-type manganese dioxide nanofibers. J. Phys. Chem. C 112 (2008) 13134-13140.

[57] C.M. Julien, M. Massot, C. Poinsignon, Lattice vibrations of manganese oxides. I. Periodic structures. Spectrochim. Acta A 60 (2004) 689-700.

[58] C. Julien, M. Massot, R. Baddour-Hadjean, S. Franger, S. Bach, J.P. Pereira-Ramos, Raman spectra of birnessite manganese dioxides. Solid State Ionics 159 (2003) 345–356.

[59] J. Dai, S.F.Y. Li, K.S. Siow, Z. Gao, Synthesis and characterization of the hollandite-type MnO_2 as a cathode material in lithium batteries. Electrochim. Acta 45 (2000) 2211-2217.

[60] L.I. Hill, A. Verbaere, D. Guyomard, MnO_2 (α-, β-, γ-) compounds prepared by hydrothermal-electrochemical synthesis: characterization, morphology, and lithium insertion behavior. J. Power Sources 119-121 (2003) 226-231.

[61] C. Zhang, C. Feng, P. Zhang, Z. Guo, Z. Chen, S. Li, H. Liu, $K_{0.25}Mn_2O_4$ nanofiber microclusters as high-power cathode materials for rechargeable lithium batteries. RSC Adv. 2 (2012) 1643-1649.

[62] E. Sarasketa-Zabala, F. Aguesse, I. Villareal, L.M. Rodriguez-Martinez, C.M. Lopez, P. Kubiak, Understanding lithium inventory loss and sudden performance fade in cylindrical cells during cycling with deep-discharge steps. J. Phys. Chem. C 119 (2015) 896-906.

[63] C.S. Johnson, D.W. Dees, M.F. Mansuetto, M.M. Thackeray, D.R. Vissers, D. Argyriou, C.K. Loong, L.J. Christensen, Structural and electrochemical studies of α-manganese dioxide (α-MnO_2). J. Power Sources 68 (1997) 570-577.

[64] A. Esmanski, G.A. Ozin, Silicon inverse-opal-based microporous materials as negative electrodes for lithium ion batteries. Adv. Funct. Mater. 19 (2009) 1999-2010.

[65] D. A. Tompsett, M. S. Islam, Electrochemistry of hollandite α-MnO_2: Li-ion and Na-ion insertion and Li_2O incorporation. Chem. Mater. 25 (2013) 2515-2526.

[66] R. Ma, Y. Bando, L. Zhang, T. Sasaki, Layered MnO_2 nanobelts: hydrothermal synthesis and electrochemical measurements. Adv. Mater. 16 (2004) 918-922.

[67] X. Huang, D. Lv, Q. Zhang, H. Chang, J. Gan, Y. Yang, Highly crystalline macroporous β-MnO_2: hydrothermal synthesis and application in lithium battery. Electrochim. Acta 55 (2010) 4915-4920.

[68] F. Cheng, J. Zhao, W. Song, C. Li, H. Ma, J. Chen, P. Shen, Facile controlled synthesis of MnO_2 nanostructures of novel shapes and their application in batteries. Inorg. Chem. 45 (2006) 2038-2044.

[69] Y. Yang, L. Xiao, Y. Zhao, F. Wang, Hydrothermal synthesis and electrochemical characterization of α-MnO_2 nanorods as cathode material for lithium batteries. Int. J. Electrochem. Sci. 3 (2008) 67-74.

[70] K.M. Shaju, G.V. Subba-Rao, B.V.R. Chowdari, EIS and GITT studies on oxide cathodes, O2-$Li_{2/3+x}(Co_{0.15}Mn_{0.85})O_2$ (x=0 and 1/3). Electrochim. Acta 48 (2003) 2691-2703.

[71] X. Zhang, A. Mauger, Q. Lu, H. Groult, L. Perrigaud, F. Gendron, CM. Julien, Synthesis and characterization of $LiNi_{1/3}Mn_{1/3}Co_{1/3}O_2$ by wet-chemical method. Electrochim. Acta 55 (2010) 6440-6449.

[72] Y. Yuan, S.M. Wood, K. He, W. Yao, D. Tompsett, J. Lu, A. Nie, M.S. Islam, R. Shahbazian-Yassar, Atomistic insights into the oriented attachment of tunnel-based oxide nanostructures. ACS Nano 10 (2016) 539-548.

[73] B.W. Byles, N.K.R. Palapati, A. Subramanian, E. Pomerantseva, The role of electronic and ionic conductivities in the rate performance of tunnel structured manganese oxides in Li-ion batteries. APL Mater. 4 (2016) 046108.

[74] E. Cockayne, L. Li, First-principles DFT+U studies of the atomic, electronic, and magnetic structure of α-MnO_2 (cryptomelane). Chem. Phys. Lett. 544 (2012) 53–58.

[75] J. Vondrak, I. Jakubec, J. Bluska, Electrochemical insertion of lithium in manganese dioxide. J. Power Sources 14 (1985) 141-147.

[76] S. Bach, J.P. Pereira-Ramos, N. Baffier, A new MnO_2 tunnel related phase as host lattice for Li intercalation. Solid State Ionics 80 (1995) 151-158.

[77] P. G. Dickens, G.J. Reynolds, Transport and equilibrium properties of some oxide insertion compounds. Solid State Ionics 5 (1981) 331-334.

[78] N. Kumagai, T. Sasaki, S. Oshitari, S. Komaba, Characterization and lithium insertion characteristics of hollandite-type $K_y(Mn_{1-x}M_x)O_2$ for rechargeable lithium battery electrodes. J. New Mater. Electrochem. Syst. 9 (2006) 175–180.

[79] Y. Kadoma, S. Oshitari, K. Ui, N. Kumagai, Characterization and electrochemical properties of Li^+ ion-exchanged products of hollandite-type $K_y(Mn_{1-x}Co_x)O_2$ for rechargeable lithium battery electrodes. Solid State Ionics 179 (2008) 1710–1713.

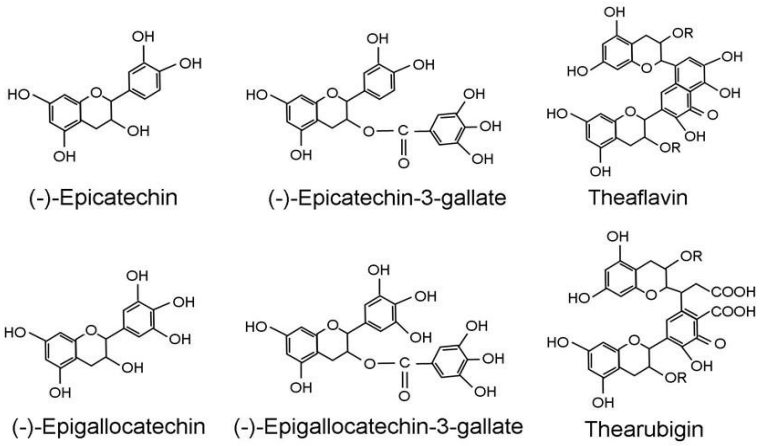

Fig. 1. The chemical structures of the major flavonoids found in both green and black tea [32]. R=Galloyl group.

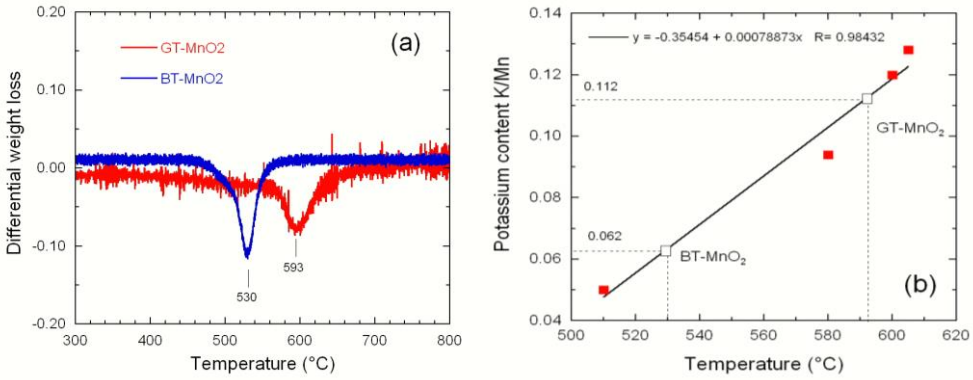

Fig. 2. (a) Plots of the derivative weight loss vs. temperature showing the decomposition of MnO_2 to Mn_2O_3 at T>500 °C. (b) The concentration of K^+ ions in the (2×2) tunnels of the α-K_xMnO_2 frameworks vs. the decomposition temperature. The linear relationship was established from experimental data by Hashem et al. [21] and Poyraz et al. [38].

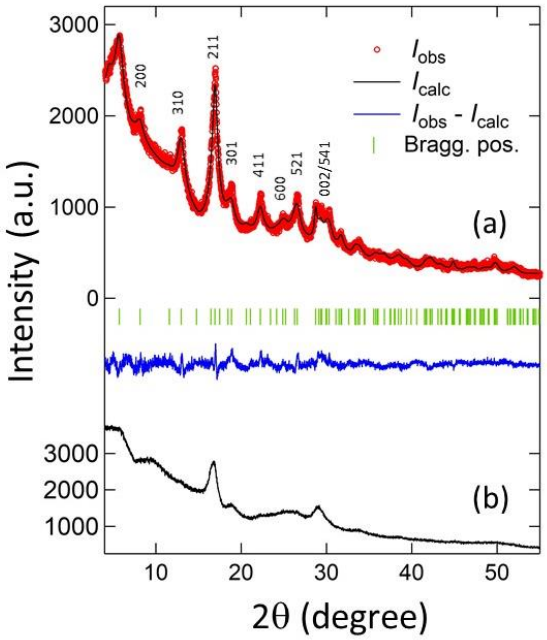

Fig. 3. Rietveld refinement of GT-MnO_2 (a) and XRD diffraction pattern of BT-MnO_2 showing much poorer crystallinity.

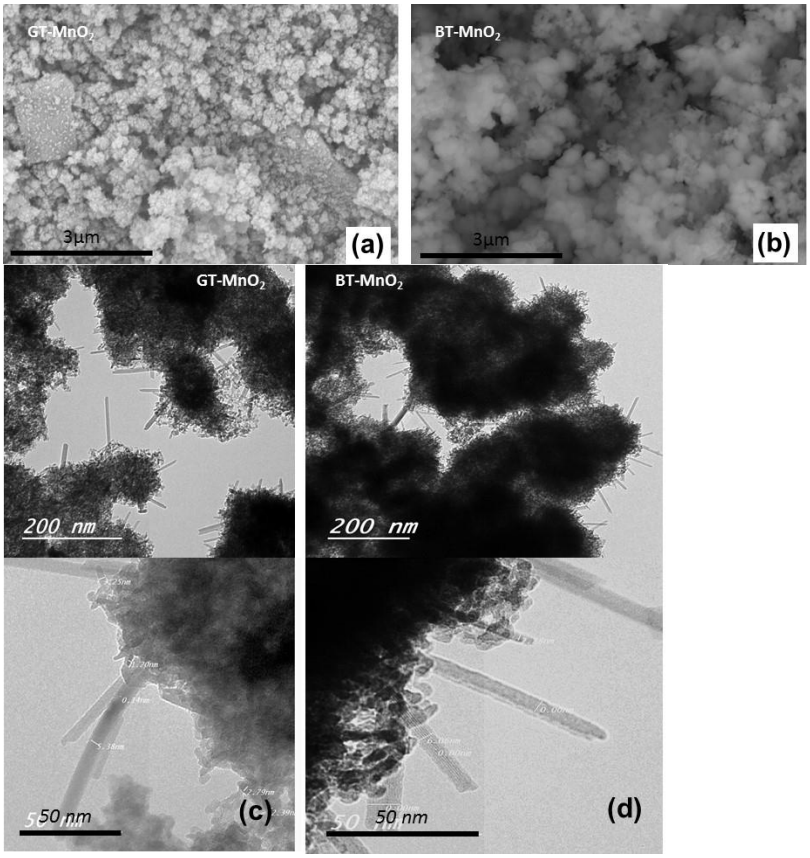

Fig. 4. SEM images (a,b) and TEM images (c,d) of GT-MnO_2 and BT-MnO_2.

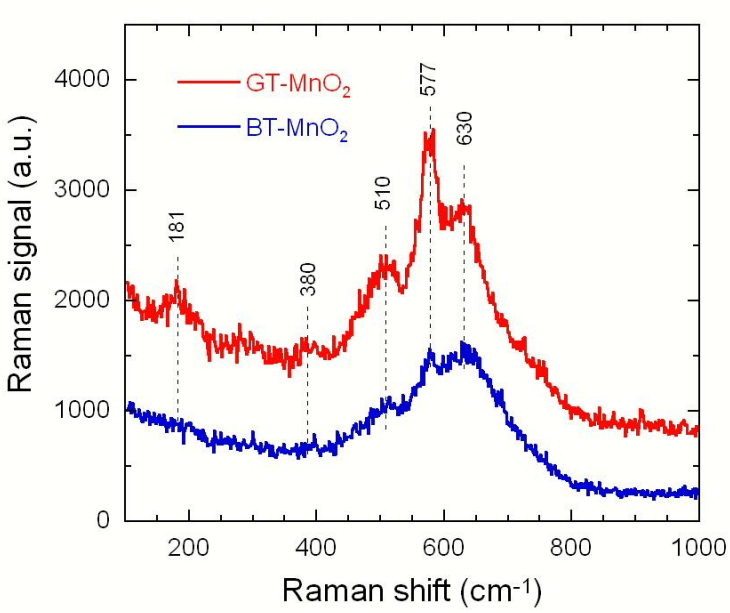

Fig. 5. Raman scattering spectra of GT-MnO_2 and BT-MnO_2 α-phase recorded using a 523 nm laser excitation.

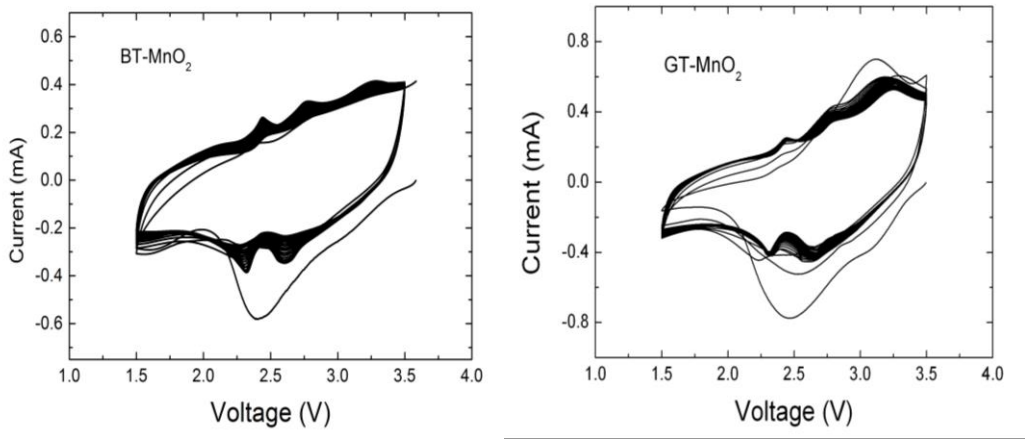

Fig. 6. Cyclic voltammograms carried out at scan rate of 0.1 mV s^{-1} in the potential range 1.5-3.5 V vs. Li^{+}/Li^{0}.

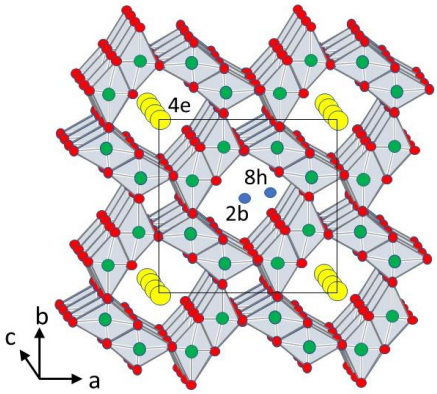

Fig. 7. Crystal structure of α-MnO_2 showing insertion sites at Wyckoff position 4*e*, 8*h* and 2*b*. The 8*h* (*x*,*y*,0) and 2*b* (0,0,½) sites are coplanar by adding the centering (½,½,½) planes perpendicular to the *c*-axis, while the 4*e* site is located at a general position (0,0,*z*). Small (red) spheres are oxygen, large (green) spheres are Mn cations inside the MnO_6 octahedra, and yellow spheres are potassium cations.

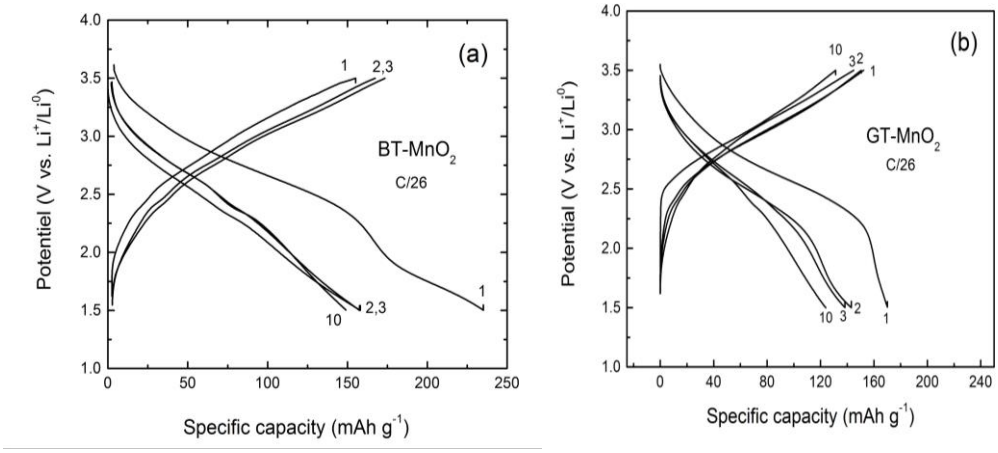

Fig. 8. Discharge-charge profiles of MnO_2//Li cells including (a) BT-MnO_2 and (b) GT-MnO_2 as positive electrode materials recorded at current density 10 mA g^{-1} (C/26) in the potential range 1.5–3.5 V vs. Li^+/Li^0.

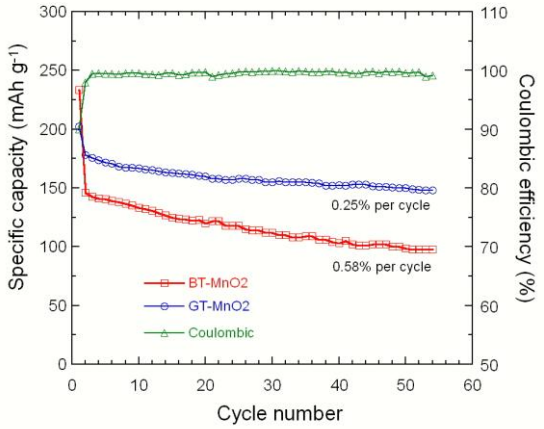

Fig. 9. Cycling performance cycled at constant current density 20 mA g^{-1} (≈C/10) in the potential range 1.5-3.5 V vs. Li^+/Li^0 and coulombic efficiency of GT-MnO_2 and BT-MnO_2.

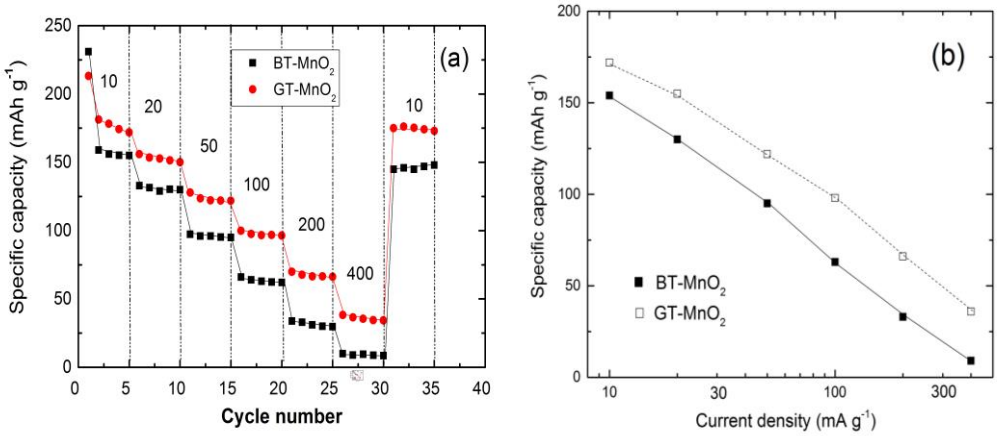

Fig. 10. (a) Rate capability at various current densities from 10 to 400 mA g^{-1} (1C=260 mA g^{-1}) and (b) Modified Peukert plots for GT-MnO_2 and BT-MnO_2 electrodes.

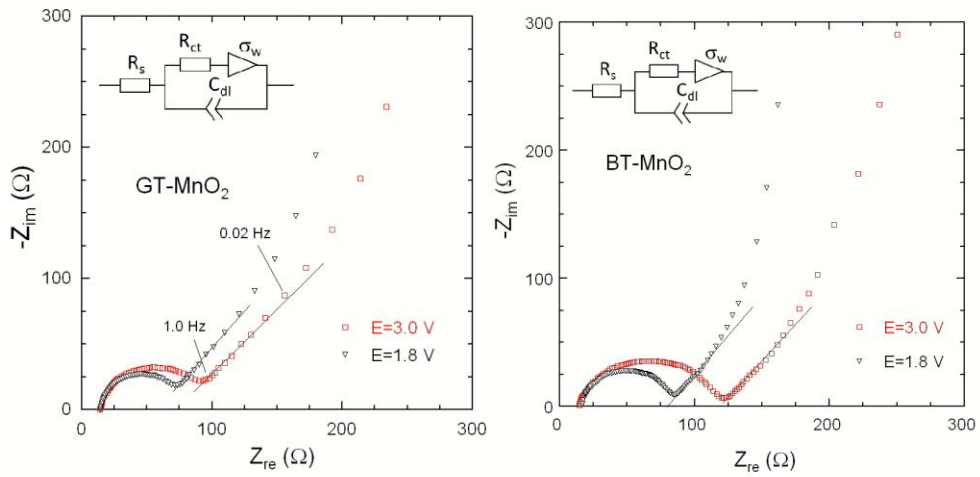

Fig. 11. EIS spectra of GT-MnO_2 and BT-MnO_2 electrodes as a function of the cell potential E=3.0 V (x≈0.05) and E=1.8 V (x≈0.6).

Table 1. Potassium content filling the 2×2 tunnel of K_xMnO_2 estimated from TG analysis.

Sample	Decomposition temperature (°C)	K^+ content
GT-MnO_2	593±2	0.11(2)
BT-MnO_2	530±2	0.06(2)

Table 2. Lattice parameters of the $K_{0.135}MnO_2$ sample (space group *I*4/*m*) prepared with lemon juice and lemon peel as reducing agents. Rietveld refinements were performed by the FULLPROF program.

Parameter	P-MnO_2
a (Å)	9.826(7)
b (Å)	9.826(7)
c (Å)	2.845(2)
V (Å^3)	274.1 (3)
Crystallite size (nm)	2.5(5)
R_{wp}	18.6
χ^2	1.75

Table 3. The surface and pore characteristics of MnO_2 powders.

Compound	S_{BET} ($m^2\ g^{-1}$)	Pore volume ($cm^2\ g^{-1}$)	Mean pore size (nm)
GT-MnO_2	49.8	0.066	11.5
BT-MnO_2	33.2	0.054	7.7

Table 4. Redox potentials recorded by cyclic voltammetry for GT-MnO_2 and BT-MnO_2 α-phases.

Material	Cathodic potential at 1st cycle (V)	Redox potentials at 2nd and subsequent cycles	
		Reduction	Oxidation
BT-MnO_2	2.40	2.31	2.44
		2.61	2.76
GT-MnO_2	2.45	2.30	2.44
		2.65	2.80

Table 5. Randles parameters and diffusion coefficient D_{Li+} of GT- and BT-MnO_2 electrodes.

Electrode	Cell voltage(V)	R_s (Ω)	R_{ct} (Ω)	σ_w (Ω $s^{-1/2}$)	D_{Li+} (cm^2 s^{-1})
GT-MnO_2	3.0	14.5	83.2	40.2	5.2×10^{-11}
	1.8	14.3	60.2	45.9	4.0×10^{-11}
BT-MnO_2	3.0	16.5	105.8	63.1	2.1×10^{-11}
	1.8	16.0	67.9	74.0	1.5×10^{-11}